Journal of Solid State Chemistry 182 (2009) 457–464

Contents lists available at ScienceDirect

Journal of Solid State Chemistry

journal homepage: www.elsevier.com/locate/jssc

Anomalous lattice parameter increase in alkali earth aluminium substituted tungsten defect pyrochlores

Gordon J. Thorogood [a,b,*], Brendan J. Kennedy [b], Vanessa K. Peterson [c], Margaret M. Elcombe [c], Gordon J. Kearley [c], John V. Hanna [a], Vittorio Luca [a]

[a] Institute of Materials Engineering, Australian Nuclear Science and Technology Organisation (ANSTO), Lucas Heights, NSW 2234, Australia
[b] School of Chemistry, University of Sydney, Sydney, NSW 2006, Australia
[c] Bragg Institute, Australian Nuclear Science and Technology Organisation (ANSTO), Lucas Heights, NSW 2234, Australia

ARTICLE INFO

Article history:
Received 15 August 2008
Received in revised form
23 October 2008
Accepted 2 November 2008
Available online 20 November 2008

Keywords:
Oxides
Neutron scattering
X-ray diffraction
Modelling
VASP
Solid state NMR

ABSTRACT

The structures of the defect pyrochlores $AAl_{0.33}W_{1.67}O_6$ where A = K, Rb or Cs have been investigated using X-ray and neutron powder diffraction methods as well as the ab initio modelling program VASP. The three cubic pyrochlores exhibit a non-linear increase in lattice parameter with respect to ionic radius of the A cation as a consequence of displacive disorder of the A-type cations. Solid state ^{27}Al MAS NMR studies of this pyrochlore system reveal shifts in the $\delta\sim$21–22 ppm range that are indicative of pseudo-5 coordinate Al environments and emanate from distorted Al octahedral with one abnormally long Al–O bond. Solid state ^{39}K, ^{85}Rb, ^{87}Rb and ^{133}Cs MAS and static NMR studies reflect the local cation disorder demonstrated in the structural studies.

1. Introduction

Oxides exhibiting the pyrochlore structure display a large variety of physical properties including catalytic activity, piezoelectric behaviour, ferro- and ferrimagnetism, and giant magnetoresistance [1,2]. Other pyrochlores exhibit a range of electrical and ionic conductivities [3], that include metallic, semiconducting and superconductivity [4,5]. Because pyrochlores possess such a wide range of properties they have been utilised in many applications including the immobilisation and treatment of nuclear waste [6,7]. Pyrochlores have also been reported to undergo order/disorder transformations upon heating [8]; this property is potentially important as the amount of disorder of the A cation may have an influence on the ion exchange properties of the material.

The general formula of pyrochlore oxides is $A_2B_2O_7$, although this can also be written as $A_2B_2O_6O'$ or B_2O_6 A_2O' to highlight the two interpenetrating networks [1]. The corner-shared BO_6 octahedra form a B_2O_6 network that intersects with A–O′ chains of formula A_2O'. These two networks only interact weakly and vacancies in the A_2O' network are common place and defect pyrochlores such as $Pb_2Ru_2O_{6.5}$ [9] KOs_2O_6 [5], and $(NH_4)NbWO_6$ [10] are regularly encountered. In these defect pyrochlores the A-type cations bond to six-oxygen atoms from the puckered hexagonal rings formed by the B_2O_6 network. Charge balance of the pyrochlore can be achieved either by combinations of different valences for the A and B cations, or by vacancies in the A_2O' network. It is this compositional flexibility of the pyrochlore structure that makes these oxides potentially attractive for many applications in materials chemistry.

The ideal $A_2B_2O_6O'$ pyrochlore structure has cubic $Fd\bar{3}m$ symmetry with each of the four atoms occupying special positions, the A-type cations on 16c at $(\frac{1}{2},\frac{1}{2},\frac{1}{2})$, the B cations on 16d at (0,0,0), the O on 48f at $(x,\frac{1}{8},\frac{1}{8})$ and O′ on 8b at $(\frac{3}{8},\frac{3}{8},\frac{3}{8})$. In a number of recent studies, including that of Whittle et al. [7] of the defect pyrochlores $CsB_{0.5}W_{1.5}O_6$ (B=Ti, Zr, Hf), displacive disorder of the A-cations in the ⟨111⟩ planes has been observed [11–18].

The importance of such disorder is now being realised. For example displacive disorder is believed to contribute to the high relative permittivities displayed by $(Bi,Zn)_2(Zn,Nb)_2O_7$ that makes these materials attractive for use as capacitors [11,12]. Neutron and X-ray diffraction studies suggest that the disorder involves displacement of the A-cation along the six ⟨112⟩ or

* Corresponding author at: Institute of Materials Engineering, Australian Nuclear Science and Technology Organisation (ANSTO), Lucas Heights, PMB 1, Menai, NSW 2234, Australia. Fax: +61 2 9543 7179.
E-mail address: gordon.thorogood@ansto.gov.au (G.J. Thorogood).

0022-4596/$ - see front matter © 2008 Elsevier Inc. All rights reserved.
doi:10.1016/j.jssc.2008.11.014

〈110〉 directions [14–16]. Previously we have described diffuse scattering in electron diffraction patterns of $CsTi_{0.5}W_{1.5}O_6$ pyrochlores [19] that suggests there are strong local correlations among the disordered ions. Withers has suggested that the $O'A_4$ tetrahedra within the pyrochlore average structure type rotate as essentially rigid bodies with the O′ anions remaining in the centre of the tetrahedra [14].

Movement of the 48*f* O anion away from $x=\frac{3}{8}$ reduces the interaction between the two networks and so may influence the magnitude of the displacive disorder of the *A*-cation. The synthesis of $AAl_{0.33}W_{1.67}O_6$ was first reported by Le Flem et al. [20] and $KAl_{0.33}W_{1.67}O_6\cdot nH_2O$ was included in the study of $KB_xW_{2-x}O_6$ (B = Al, Ti and Ta) oxides by Subramanian et al. [21]. The aim of our work was to examine the nature of the *A* cation disorder with respect to ionic radius in the series $AAl_{0.33}W_{1.67}O_6$ (where A = K, Rb, Cs) and to establish if this is correlated with the movement or displacement of the O′ at the 8*b* position, and to probe the possibility of local (short-range) ordering between the Al and W cations. The ionic radius, *r*, of K^+ with 8-fold coordination is 1.51 Å and this increases, essentially linearly down group 1, Rb^+ is 1.61 Å and Cs^+, 1.74 Å. The X-ray diffraction patterns reveal a non-linear increase in the *a* lattice parameter as the *A*-cation size was increased in the pyrochlore $AAl_{0.33}W_{1.67}O_6$. We have used a combination of neutron and X-ray diffraction data in a joint Rietveld refinement to locate the positions of the *A* cations and 48*f* oxygen and the site occupancies of the aluminium atoms.

2. Experimental

2.1. Synthesis

The appropriate stoichiometric amounts of KNO_3, $RbNO_3$, $CsNO_3$, $Al(OH)_3$ and WO_3 were mixed, calcined in air at 500 °C, ball milled in cyclohexane for 12 h and then sintered in air or vacuum at 750 °C for 12 h. The intended stoichiometries of the samples were $KAl_{0.33}W_{1.67}O_6$, $RbAl_{0.33}W_{1.67}O_6$ and $CsAl_{0.33}W_{1.67}O_6$. Attempts were made to synthesise $Na_{0.5}K_{0.5}Al_{0.33}W_{1.67}O_6$ to access a smaller effective *A* cation radii; this material however yielded a single phase hexagonal structure and was not examined further.

2.2. TGA/DTA

Simultaneous thermogravimetric analysis (TGA) and differential thermal analysis (DTA) were performed on a Setaram TAG 24 (Setaram, France). Approximately 10 mg of each powder was placed on a platinum crucible and heated to 800 °C at a rate of 5 °C min^{-1} in flowing air.

2.3. Electron microscopy

A JEOL JSM6400 scanning electron microscope (SEM) equipped with a Noran Voyager energy-dispersive X-ray spectroscopy system (EDS) was operated at 15 keV for microstructural analysis work.

2.4. Solid state NMR

High resolution ^{27}Al, ^{133}Cs, ^{87}Rb and ^{85}Rb magic-angle-spinning (MAS) NMR data were acquired at ambient temperatures on a Bruker MSL-400 spectrometer ($B_0=9.4$ T) operating at the ^{27}Al, ^{133}Cs, ^{87}Rb and ^{85}Rb frequencies of 104.23, 52.46, 130.90 and 38.60 MHz, respectively. All one-dimensional data were acquired with single pulses (Bloch decay) using a Bruker 4 mm double-air-bearing probe using typical MAS rates of 15 kHz. For quantitative estimates of the central transition intensities to be made, the quadrupolar nature of these nuclei (^{27}Al ($I=\frac{5}{2}$), ^{133}Cs ($I=\frac{7}{2}$), ^{87}Rb ($I=\frac{3}{2}$), ^{85}Rb ($I=\frac{5}{2}$)) necessitated that flip angles be close to the condition [22,23]

$$(I+\tfrac{1}{2})\omega_{rf}t_p\leqslant\pi/6$$

For the ^{27}Al MAS NMR measurements, a non-selective $\pi/2$ pulse time of 5.0 μs was measured on a 1.0 M $Al(NO_3)_3$ solution from which a selective pulse time of 0.6 μs was selected for data acquisition on all solid samples. Relaxation delays of 3 s were typically used; the quantification and speciation of these data were verified with experiments that had delays extending to 30 s. All ^{27}Al chemical shifts were referenced to 1.0 M $Al(NO_3)_3$ that was set to δ 0.0 ppm. The ^{133}Cs MAS NMR pulse conditions were calibrated on 1.0 M CsCl solution from which a non-selective $\pi/2$ pulse time of 6 μs was measured, with a subsequent selective pulse time of 0.6 μs employed for data acquisition. Typical relaxation delays were 3 s, however checks for abnormally long T_1s were undertaken with recycle delays of up to 60 s being implemented. All ^{133}Cs chemical shifts were referenced to 1 M CsCl that was set to δ 0.0 ppm. Similar ^{87}Rb and ^{85}Rb MAS NMR experiments were performed, with pulse conditions for these nuclei being calibrated on solid RbCl. For the ^{87}Rb measurements, a non-selective $\pi/2$ pulse time of 3.5 μs from which a selective pulse time of 0.6 μs was used, while the ^{85}Rb measurements were calibrated with a non-selective $\pi/2$ pulse time of 6.0 μs from which a selective pulse time of 0.6 μs was chosen. Relaxation delays of 3 s were employed for these nuclei, with both ^{87}Rb and ^{85}Rb chemical shifts being referenced to 0.01 M RbCl via the secondary solid RbCl standard (δ 126.8 ppm).

Static (broadline) ^{39}K NMR data were acquired at a ^{39}K frequency of 18.67 MHz. Data was acquired in a standard dual-channel 7.5 mm solenoid coil probe with the θ–τ_1–θ–τ_2-acquire solid echo sequence with an extended phase cycle to minimise echo distortion [24]. A non-selective $\pi/2$ pulse time of 12.0 μs was calibrated on solid KCl, from which selective θ echo pulse times of 2.0 μs were used. Relaxation delays of 5 s were implemented, with ^{39}K chemical shifts being referenced to 0.1 M KCl via the secondary solid KCl standard (δ 48.0 ppm).

Due to the disordered nature of the materials studied, all ^{27}Al, ^{133}Cs, ^{87}Rb, ^{85}Rb and ^{39}K apparent shifts δ are reported as centre-of-gravity measurements and remain uncorrected for second order quadrupolar effects unless specifically reported as isotropic chemical shift values δ_{iso} obtained from simulation or graphical methods.

2.5. X-ray diffraction

Powder X-ray diffraction measurements were made using a Panalytical X'Pert Pro X-ray diffractometer equipped with a Real Time Multiple Strip (RTMS) X'celerator detector covering a solid angular range of 2° at 25 °C using Cu*K*α radiation, a flat-plate sample holder and an Anton Paar TTK 450 sample cell. Data of sufficient quality for structural refinement were collected over $10^\circ<2\theta<80^\circ$, in 0.017° steps, with an equivalent acquisition time of 1000 s per step. Structures were refined by the Rietveld method using the program RIETICA [25].

2.6. Neutron diffraction

Neutron powder diffraction data were collected, during commissioning, on Wombat, the high intensity powder diffractometer at the Open Pool Australian Light water reactor (OPAL) facility at the Australian Nuclear Science and Technology Organisation (ANSTO) [26]. Room temperature data was acquired

over 3 min using an area detector from $22.75^\circ < 2\theta < 142.55^\circ$, pixel spacing 0.125°. The incident wavelength was 1.2212(1) Å determined using the NIST Al_2O_3 standard, which refined with well acceptable crystallographic parameters. The data had the background from an empty can subtracted before correction for detector efficiency determined from a vanadium pattern. A curvature correction algorithm was then applied to the data, and the data were reduced to 1 dimension by vertically summing over the central third of the area detector.

2.7. Modelling

Modelling of the system was performed by ab initio quantum–mechanical density functional theory (DFT) via the Vienna Ab initio Simulation Package (VASP). For our purposes we used VASP 4.6 planewave DFT code running on ACAPAC SGI Altix 3700B × 2 cluster. This configuration used 32 nodes and took between 1 and 5 h real time per energy minimisation. Minimisation was achieved using a quasi-Newton algorithm with all atoms free to relax, but the unit-cell parameters constrained to the experimental values. Characteristics of the simulation were as follows: Two *k*-points (000,111) in reciprocal space. Energy cutoff = 600 eV; Convergence for the self-consistent field (SCF) was 1.0×10^{-6} eV; Convergence limit for energy minimisation was 1.0×10^{-7} eV; The Perdew–Burke–Ernzerhof (PBE) exchange correlation functional was used along with projector augmented wave (PAW) pseudopotentials.

3. Results

3.1. Characterisation

TGA shows a ~1.4% weight loss for the $KAl_{0.33}W_{1.67}O_6$ sample and ~0.4% weight loss for $RbAl_{0.33}W_{1.67}O_6$ and $CsAl_{0.33}W_{1.67}O_6$, indicating that there is a small amount of water associated with the structure of $KAl_{0.33}W_{1.67}O_6$, Fig. 1. The uptake of H_2O by $KAl_{0.33}W_{1.67}O_6$ has been previously reported by Subramanian et al. [21] although in that study $KAl_{0.33}W_{1.67}O_6$ was reported to contain only 0.9% H_2O, $\sim\frac{2}{3}$ of the value seen in the current study. The percentage weight loss of 1.4% is equivalent to an *n* value of ~0.35 if the formula is written as $KAl_{0.33}W_{1.67}O_6 \cdot nH_2O$.

The change in slope of the $KAl_{0.33}W_{1.67}O_6$ data at ~150 °C is thought to be related to the kinetics of dehydration, most of the water has been removed from the structure at this point. Subramanian et al. [21] reported that $KAl_{0.33}W_{1.67}O_6$ could be fully dehydrated by heating to 125 °C. No phase change was observed over the temperature range investigated.

3.2. Diffraction

Analysis of the X-ray diffraction patterns from the three samples shows that they do not display a linear increase in the *a* lattice parameter, with respect to *A* cation size (Fig. 2). This is contrary to the results reported by Le Flem et al. [20] although Le Flem did not account for the adsorption of H_2O in the sample containing K. This trend in lattice parameter is counter intuitive as the ionic radii increases, essentially linearly, down group 1 from 1.51 Å in K^+ to 1.61 Å for Rb^+ and 1.74 Å in Cs^+. The possibility that the increased lattice parameter in $KAl_{0.33}W_{1.67}O_6.0.35H_2O$ is solely a consequence of the absorbed water was discounted by measurements after dehydrating the sample at 200 °C for 30 min. It can be clearly seen in Fig. 2 that the lattice parameters still do not vary linearly with ionic radii.

Phase analysis of the X-ray diffraction patterns from each of the compounds indicate slight contaminant phases in some of the materials, the results of which are summarised in Table 1. It is evident from this table that only for $RbAl_{0.33}W_{1.67}O_6$ was it not possible to prepare single phase samples. Analytical microscopy results of the $RbAl_{0.33}W_{1.67}O_6$ sample yielded a stoichiometry of the major pyrochlore phase in agreement with the desired composition.

The structures of the three samples were refined in space group $Fd\bar{3}m$ using a combination of powder X-ray and neutron

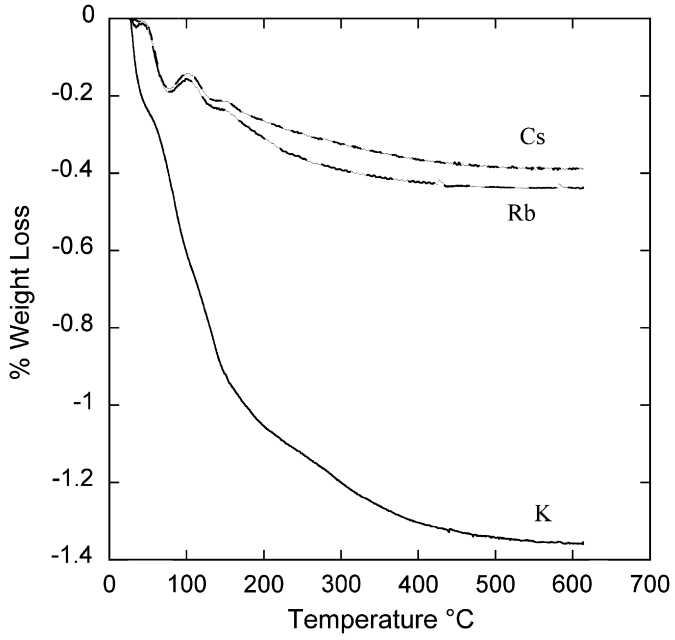

Fig. 1. Plot of weight loss versus temperature for $KAl_{0.33}W_{1.67}O_6$ (K), $RbAl_{0.33}W_{1.67}O_6$ (Rb), and $CsAl_{0.33}W_{1.67}O_6$ (Cs). The small anomalies in the $RbAl_{0.33}W_{1.67}O_6$ and $CsAl_{0.33}W_{1.67}O_6$ data at ~100 and ~150 °C are an instrumental artefact.

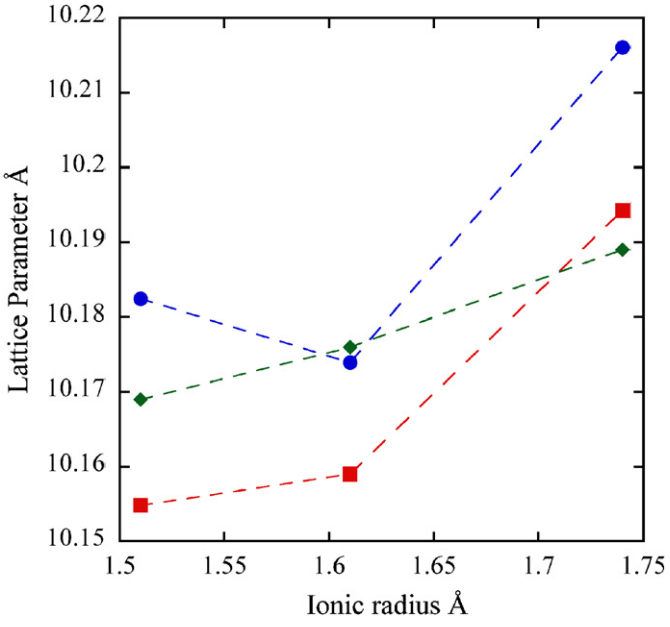

Fig. 2. Plot of *a* lattice parameter versus ionic radius for $AAl_{0.33}W_{1.67}O_6 \cdot nH_2O$. The circles are from the as-prepared samples and the squares after drying at 200 °C for 30 min. The diamonds are the results from La Flem [20]. The larger difference between the as-prepared and dried samples reflects the greater water content in this sample. Note error bars are smaller in dimension than data point markers.

Table 1
Stoichiometry attempted at various environments and resultant phases, estimated using powder X-ray diffraction.

Stoichiometry	Air sinter, phases present	Vacuum sinter in quartz, phases present
$Na_{0.5}K_{0.5}Al_{0.33}W_{1.67}O_6$	Hexagonal $Na_{0.5}K_{0.5}Al_{0.33}W_{1.67}O_6$	Unknown Na3AlW3O12 ~50% Hexagonal $Na_{0.5}K_{0.5}Al_{0.33}W_{1.67}O_6$ ~50%
$KAl_{0.33}W_{1.67}O_6$	Pyrochlore $KAl_{0.33}W_{1.67}O_6$	Hexagonal $KAl_{0.33}W_{2.67}O9$ ~10% Unknown $K_2W_4O_{13}$ ~90%
$RbAl_{0.33}W_{1.67}O_6$	Pyrochlore $RbAl_{0.33}W_{1.67}O_6$ ~95% Orthorhombic $Rb_{15}W_{45.5}O_{144}$ ~5%	Pyrochlore $RbAl_{0.33}W_{1.67}O_6$ ~75% Orthorhombic $Rb_{15}W_{45.5}O_{144}$ ~25%
$CsAl_{0.33}W_{1.67}O_6$	Pyrochlore $CsAl_{0.33}W_{1.67}O_6$ ~98% Cubic Cs_2O ~2%	Pyrochlore $CsAl_{0.33}W_{1.67}O_6$

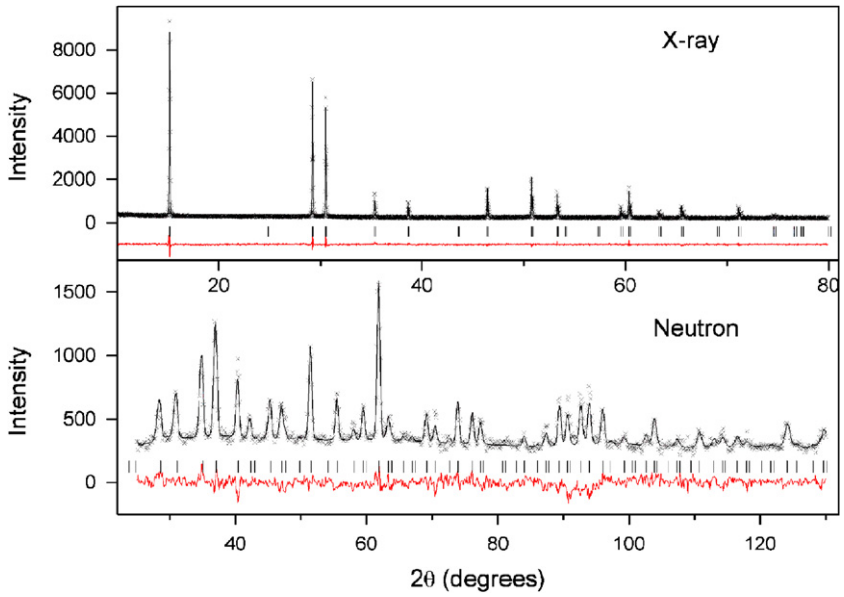

Fig. 3. Top: Observed (crosses), calculated and difference (lower solid line) X-ray diffraction patterns of $KAl_{0.33}W_{1.67}O_6$ sintered in air. The vertical black markers show the positions of the Bragg reflections. Below: Neutron Diffraction data of $KAl_{0.33}W_{1.67}O_6$ sintered in air. The higher than expected background is due to the presence of water in the sample.

diffraction data (Fig. 3). In these refinements the W and Al were assumed to statistically occupy the 16*c* site.

In the refined model the *A*-cation was initially located at the 8*b* site at $\frac{3}{8},\frac{3}{8},\frac{3}{8}$. This is positioned in the centre of the channels running along the [111] direction and places the *A*-type cation mid-way between two puckered O_6 hexagons. Invariably this model resulted in unacceptably high displacement parameters, $B_{iso} > 5\,Å^2$. Equally important the Bond Valence Sums of the *A*-cation was unacceptably low (approximately less than 0.77) although that of the W and Al appeared reasonable. Recall that there are two common reasons for the observation of large atomic displacement parameters, namely the presence of vacancies or the displacement of the atom away from the designated site. *A*-cation vacancies should not impact on the BVS of the *A*-type cations. Further the analytical microscopy did not indicate the existence of appreciably non-stoichiometry of the *A*-cation. Consequently the occupancy of this was fixed at the nominal stoichiometry in the refinements. A number of displacement models were investigated including placing *A* at $0,x,\bar{x}$ and the most stable results were obtained if *A* was placed at *x*, *x*, *x* with $x \sim 0.3445$ for the K compound, similar results were obtained for the other two oxides studies. There is some water in the structures as evident from the TGA studies and the contraction in the lattice upon heating. The neutron diffraction data were not of sufficient quality to establish the precise position of these small amounts of water.

Selected atomic parameters and inter-atomic distances from the refinements are given in Table 2 and 3. It is possible that short range order of the Al/W cations is responsible for the larger than typical displacement parameters for the 16*c* cations.

The refined value of *x* for the O(1) site indicates compression of the octahedra in the [111] direction. The displacements of the *A*-type cation from the 8*b* site at $(\frac{333}{888})$ decreased as the size of the *A*-cation increased K < Rb < Cs, illustrating that the A cation radius had a systematic impact.

3.3. Electron microscopy

The scanning electron micrographs showed the samples contain well shaped single crystals, together with variable amounts of less well structured material. These particles were ~10 μm in size and an example of which is given in Fig. 4. Analytical microscopy suggested that the air sintered K sample and the vacuum sintered Cs sample only contained the pyrochlore

Table 2
Selected atomic parameters for the most phase pure samples.

Atom/site	x	y	z	N	$B(iso)$ Å^2
$KAl_{0.33}W_{1.67}O_6$ $a = 10.1808(1)$ Å					
K 32*e*	0.3445(6)	0.3445(6)	0.3445(6)	0.038	3.3(5)
Al 16*c*	0.000	0.000	0.000	0.007	3.45(4)
W 16*c*	0.000	0.000	0.000	0.069	3.45(4)
O 48*f*	0.3121(2)	0.125	0.125	0.2500	1.12(4)
$RbAl_{0.33}W_{1.67}O_6$ $a = 10.1726(2)$ Å					
Rb 32*e*	0.3569(3)	0.3569(3)	0.3569(3)	0.038	3.1(4)
Al 16*c*	0.000	0.000	0.000	0.007	3.90(5)
W 16*c*	0.000	0.000	0.000	0.069	3.90(5)
O 48*f*	0.3120(2)	0.125	0.125	0.2500	1.13(3)
$CsAl_{0.33}W_{1.67}O_6$ $a = 10.207(1)$ Å					
Cs 32*e*	0.3618(7)	0.3618(7)	0.3618(7)	0.038	1.8(8)
Al 16*c*	0.000	0.000	0.000	0.007	3.4(1)
W 16*c*	0.000	0.000	0.000	0.069	3.4(1)
O 48*f*	0.3106(3)	0.125	0.125	0.2500	1.09(4)

K (XRD) $R_{wp} = 6.97\%$, and $R_p = 5.53\%$ (ND) $R_{wp} = 8.92\%$, and $R_p = 7.06\%$; Rb (XRD) $R_{wp} = 5.67\%$, and $R_p = 4.51\%$(ND) $R_{wp} = 10.93\%$, and $R_p = 8.47\%$; Cs (XRD) $R_{wp} = 6.73\%$, and $R_p = 5.25\%$ (ND) $R_{wp} = 14.47\%$, and $R_p = 10.76\%$.

Table 3
Selected bond angles, distances and bond valence sums (BVS) for the most phase pure samples.

Sample	Framework atoms			
$KAl_{0.33}W_{1.67}O_6$	W–O[a]	× 6	1.9076 (8) Å	BVS W 6.29(1)
	W–O–W		150.23°(8)	BVS Al 3.032(7)
	K–O	× 3	2.908 (5) Å	BVS K 0.70(1)
$RbAl_{0.33}W_{1.67}O_6$	W–O	× 6	1.9059 (7) Å	BVS W 6.32(1)
	W–O–W		155.44°(2)	BVS Al 3.049(6)
	Rb–O	× 3	3.011 (3) Å	BVS Rb 0.85(1)
$CsAl_{0.33}W_{1.67}O_6$	W–O	× 6	1.9071 (9) Å	BVS W 6.29(2)
	W–O–W		155.58 °(5)	BVS Al 3.034(8)
	Cs–O	× 3	3.081 (7) Å	BVS Cs 1.18(2)

All BVS have been calculated to a maximum bond length of 4 Å.
[a] The Al distances and angles are identical to the tabulated W values.

whereas the Rb sample always contained an impurity in general agreement with phase analysis by XRD. It is possible that loss of the *A*-type cation from the nominal stoichiometric composition during calcination, under the relatively modest calcinations and sintering temperatures would promote disproportionation and the formation of a low temperature/transitional alumina such as a defect spinel-like γ-alumina. This may account for some of the decorations observed on the surface of the crystallites in Fig. 4.

3.4. VASP modelling

The crystal structure was modelled by replacing three tungsten atoms with aluminium atoms in the unit cell. This gives one excess electron which was included in the calculations, as a delocalised electron. Three distinct models were minimized—the first had two of the aluminium atoms in neighbouring octahedra, the second had a variety of Al–Al distances and the third had the Al as far apart as possible. The first model gave substantial displacement of the aluminiums towards the common oxygen giving one long, one short and four intermediate length bonds (2.00, 1.78 and 4 × 1.90 Å). In the other two models the aluminium

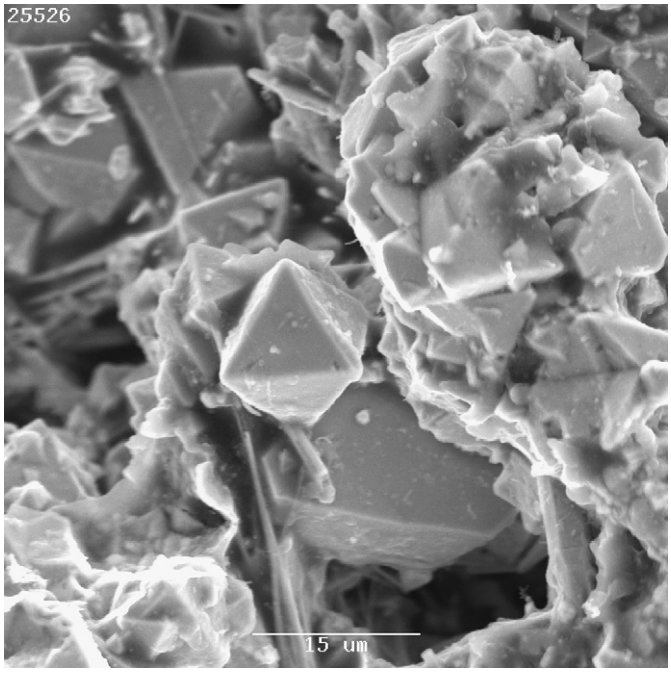

Fig. 4. SEM of $KAl_{0.33}W_{1.67}O_6$.

remained very close to the centre of the octahedra. In all models the tungsten is displaced from the centre of the octahedra giving a slightly reduced bond valence sum (down by 0.2 in the Rb compound), and the A cations show a small displacement from the $(\frac{333}{888})$ position but about half that estimated from the structural refinement and not in any specific direction. Bond valence sums for the Rb at (*x*,*x*,*x*) are 0.85 where as at the $(\frac{333}{888})$ position they drop by around 10% to 0.77. All the *A*-type cations are significantly underbonded at the 8*b* site.

The atomic displacement parameters derived from the average mean square shifts across all three models are substantially smaller than the refined values ($\sim\frac{1}{3}$).

This discrepancy is believed to be sample dependent (some samples had traces of water and the structure of the standard Al_2O_3 reference refined to acceptable values). Better statistics and/or resolution will be needed to determine if this discrepancy is real.

3.5. Multinuclear solid state MAS and static NMR

The ^{27}Al MAS NMR data of the pyrochlore series $AAl_{0.33}W_{1.67}O_6$ presented in Figs. 5(a)–(c) shows that the Al^{3+} octahedra in this structural series is characterised by a dominant narrow resonance with an apparent shift in the $\delta\sim$21–22 ppm range. This observed shift is assigned to the octahedrally coordinated Al site comprising the alumino-tungstate framework. These resonances exhibit a significant downfield shift in comparison to previously reported ^{27}Al resonances assigned to six coordinate Al positions in various condensed and intermediate aluminas and aluminium hydroxide precipitates, which are conventionally observed in the $\delta\sim$0–13 ppm range [23,27–31]. The VASP calculations described above show that where two Al (0,0,0 and 0,0,*z*) positions share a common corner they are displaced towards each other resulting in one long Al–O bond. It is thought that such a distorted octahedral configuration where the long Al–O bond is collinear with the molecular *c* axis justifies a pseudo-5 coordinate description for the Al coordination in these systems, and rationalises the large downfield shift towards the five coordinate ^{27}Al chemical shift region of $\delta\sim$25–40 ppm [23,28,30].

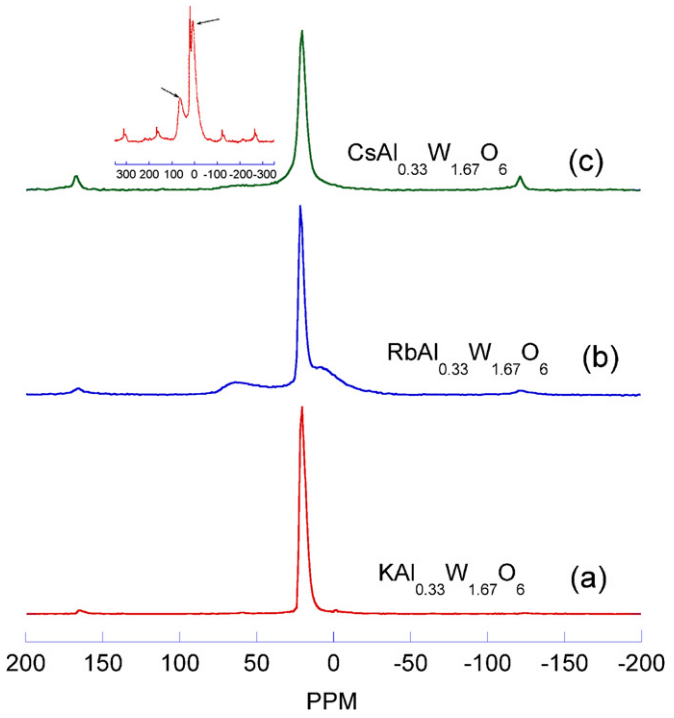

Fig. 5. ^{27}Al MAS NMR spectra of (a) $KAl_{0.33}W_{1.67}O_6$, (b) $RbAl_{0.33}W_{1.67}O_6$, and (c) $CsAl_{0.33}W_{1.67}O_6$. The insert shows example of the spectra from gamma alumina, a contaminant phase from a failed sample. The peaks identified with arrows can be seen in the spectra from the $RbAl_{0.33}W_{1.67}O_6$ sample.

Additional ^{27}Al resonances typical of six and four coordinate environments are observed at δ 8.2 ppm and δ 64.4 ppm, respectively. These are indicative of a poorly formed/highly disordered γ-alumina phase and also observed in the Rb and Cs variants. This phase was undetected in the diffraction studies, suggesting it to be amorphous, although poorly formed features were observed in the electron micrographs (see Fig. 5). An example of an incompletely reacted $CsAl_{0.33}W_{1.67}O_6$ sample is shown as an inset in Fig. 5 that demonstrates a dominance of this γ-alumina phase.

The results of the multinuclear MAS and static NMR studies of the alkali *A* cation is shown in Fig. 6. The static broadline ^{39}K measurement in Fig. 6(a) exhibits one broad featureless resonance at a shift $\delta\sim-63$ ppm. The broadening of this quadrupole dominated resonance is indicative of some local disorder that influences the K environment. Within the resolution limits of this experiment only one K site can be identified, in agreement with the X-ray and neutron structural results. This contrasts with the ^{87}Rb and ^{85}Rb MAS measurements shown in Figs. 6(b) and (c), respectively. The high resolution ^{87}Rb MAS data clearly resolves three resonances at shifts δ −28.0, −73.0 and −91.4 ppm. The narrower resonance at $\delta-91.4$ ppm is assigned to a Rb-bearing impurity phase $Rb_{15}W_{45.5}O_{144}$ and corroborates what was detected by diffraction methods at the ~5–10% level. The broader $\delta-28$ ppm and $\delta-73$ ppm resonances are associated with the $RbAl_{0.33}W_{1.67}O_6$ phase and these demonstrate two different types of cation disorder influencing the Rb speciation. The most prominent structural disorder distributes the Rb speciation between two positions or environments in an approximate ratio of ~2.5:1, as evidenced by the intensities of the $\delta-28$ ppm and $\delta-73$ ppm resonances, while more subtle local disorder is demonstrated by each resonance lineshape which exhibits some extended upfield tailing [32–35]. This observation of this phenomenon is greatly enhanced in the ^{85}Rb data by virtue of

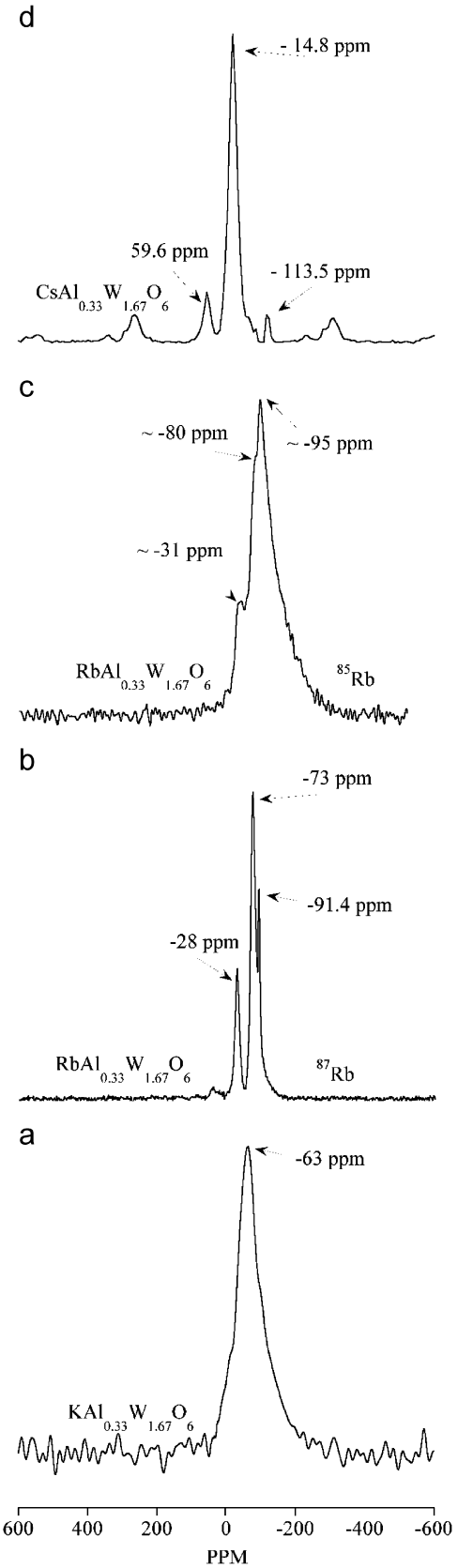

Fig. 6. (a) ^{39}K static NMR spectra of $KAl_{0.33}W_{1.67}O_6$, (b) ^{87}Rb MAS NMR spectra of $RbAl_{0.33}W_{1.67}O_6$, (c) ^{85}Rb MAS NMR spectra of $RbAl_{0.33}W_{1.67}O_6$, and (d) ^{133}Cs MAS NMR spectra of $CsAl_{0.33}W_{1.67}O_6$.

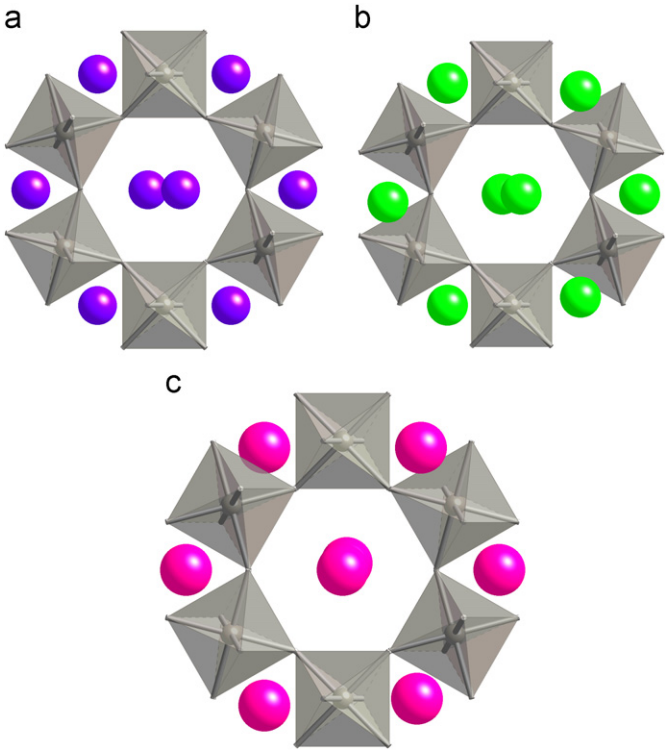

Fig. 7. Structures based on combined results of refined parameters. The purple spheres represent K (a), Rb (b) is represented by the green spheres and Cs (c) as pink. In all cases the *A*-type cation occupies 25% of all possible 32*e* sites. The magnitude of the displacement from the nearby 8*b* site can be easily seen in this [111] projection and is greatest in the K compound.

the much larger ^{85}Rb quadrupole moment Q and the reduced γ (^{87}Rb $(I=\frac{3}{2})$, $\gamma = 8.7851\times10^{7}\,\mathrm{rad\,s^{-1}\,T^{-1}}$, $Q = 0.13\times10^{-28}\,\mathrm{m^2}$; ^{85}Rb $(I=\frac{5}{2})$, $\gamma = 2.5923\times10^{7}\,\mathrm{rad\,s^{-1}\,T^{-1}}$, $Q = 0.27\times10^{-28}\,\mathrm{m^2}$), that reduces the overall ratio ν_L/ν_Q governing the spin system and consequently increases (comparatively) the quadrupolar broadening on the ^{85}Rb resonance. From Fig. 6(c) the extended tailing phenomenon on the high field side of each resonance appears quite extreme and much of the chemical shift resolution observed in the ^{87}Rb data has been lost, although similar shifts are observed from both the ^{87}Rb and ^{85}Rb data. These results suggest that a significant distribution of shifts and electric field gradients contribute to the broadening of each ^{85}Rb and ^{87}Rb resonance from the local cation positional disorder, in clear contrast to the more prominent disorder generating the chemically distinct Rb positions. A similar occurrence is observed for the high resolution ^{133}Cs MAS data of Fig. 6(d). This spectrum is dominated by a featureless resonance at $\delta-14.8$ ppm and is accompanied by resonances from Cs-bearing impurity phases at δ 56.9 ppm and δ −113.5 ppm. The very small quadrupole moment of the ^{133}Cs nucleus (^{133}Cs $(I=\frac{7}{2})$, $\gamma = 3.5339\times10^{7}\,\mathrm{rad\,s^{-1}\,T^{-1}}$, $Q = -0.003\times10^{-28}\,\mathrm{m^2}$) eliminates any significant quadrupolar contribution to the linewidths, however, the resonance is inhomogeneously broadened and a distribution of shifts is contributing to the observed linewidth, subsequently supporting the description of a locally disordered Cs position from the diffraction studies.

While the NMR studies do not allow us to establish the precise environment of the various *A*-type cations they do demonstrate an increase in disorder of these cations as their size increases, a result that is mirrored in the diffraction studies. The distribution of *A*-site environments is also likely to impact on the local order of the Al cations.

4. Conclusions

The structures of the defect $A\mathrm{Al}_{0.33}\mathrm{W}_{1.67}\mathrm{O}_6$ pyrochlores (A = K, Rb and Cs) have been investigated using diffraction (powder X-ray and neutron) spectroscopic (Solid State NMR) and modelling (VASP) methods. All the data shows the presence of displacive disorder of the *A*-type cations from the 8*b* sites at $\frac{3}{8}\frac{3}{8}\frac{3}{8}$ to a 32*e* sites at (*x*,*x*,*x*) where x = K(0.3445), Rb(0.3569) and Cs(0.3618) as illustrated in Fig. 7. Combined X-ray and neutron data sets were required to obtain accurate structural refinements of the three pyrochlores. The magnitude of the displacement of the *A*-type cation was observed to decrease as the size of the cation increased, although for all cations the magnitude of the displacement estimated from the diffraction studies was greater than that calculated.

The disorder of the *A*-type cations is correlated with the non-linear expansion of the structures observed with increase ionic radii. An important consequence of this is that the K cation effectively occupies a much larger volume than it would if it was located on the 8*b* site. This opens up the structure which in turn allows a small amount of H_2O to enter the structure. The effect of this on the favourable ion-exchange properties of $\mathrm{KAl}_{0.33}\mathrm{W}_{1.67}\mathrm{O}_6$ is the subject of on-going studies.

Acknowledgment

BJK acknowledges the support from the Australian Research Council for the work conducted at the University of Sydney.

References

[1] M.A. Subramanian, G. Aravamudan, G.V.S. Rao, Progress in Solid State Chemistry 15 (1983) 55–143.
[2] M.A. Subramanian, B.H. Toby, A.P. Ramirez, W.J. Marshall, A.W. Sleight, G.H. Kwei, Science 273 (1996) 81–84.
[3] C.A. Mims, A.J. Jacobson, R.B. Hall, J.T. Lewandowski Jr., Journal of Catalysis 153 (1995) 197–207.
[4] B.J. Kennedy, T. Vogt, Journal of Solid State Chemistry 126 (1996) 261–270.
[5] S. Yonezawa, Y. Muraoka, Y. Matsushita, Z. Hiroi, Journal of Physics: Condensed Matter 16 (2004) L9–L12.
[6] R.C. Ewing, W.J. Weber, J. Lian, Journal of Applied Physics 95 (2004) 5949–5971.
[7] K.R. Whittle, G.R. Lumpkin, S.E. Ashbrook, Journal of Solid State Chemistry 179 (2006) 512–521.
[8] K.W. Eberman, B.J. Wuensch, J.D. Jorgensen, Solid State Ionics 148 (2002) 521–526.
[9] R.A. Beyerlein, H.S. Horowitz, J.M. Longo, M.E. Leonowicz, J.D. Jorgensen, F.J. Rotella, Journal of Solid State Chemistry 51 (1984) 253–265.
[10] C.A. Perottoni, J. Haines, J.A.H. Da Jornada, Journal of Solid State Chemistry 141 (1998) 537–545.
[11] I. Levin, T.G. Amos, J.C. Nino, T.A. Vanderah, C.A. Randall, M.T. Lanagan, Journal of Solid State Chemistry 168 (2002) 69–75.
[12] T.A. Vanderah, I. Levin, M.W. Lufaso, European Journal of Inorganic Chemistry (2005) 2895–2901.
[13] B. Melot, E. Rodriguez, T. Proffen, M.A. Hayward, R. Seshadri, Materials Research Bulletin 41 (2006) 961–966.
[14] R.L. Withers, T.R. Welberry, A.K. Larsson, Y. Liu, L. Noren, H. Rundlof, F.J. Brink, Journal of Solid State Chemistry 177 (2004) 231–244.
[15] Q. Zhou, B.J. Kennedy, V. Ting, R.L. Withers, Journal of Solid State Chemistry 178 (2005) 1575–1579.
[16] W. Somphon, V. Ting, Y. Liu, R.L. Withers, Q. Zhou, B.J. Kennedy, Journal of Solid State Chemistry 179 (2006) 2495–2505.
[17] I. Ismunandar, T. Kamiyama, K. Oikawa, A. Hoshikawa, B.J. Kennedy, Y. Kubota, K. Kato, Materials Research Bulletin 39 (2004) 553–560.
[18] M. Avdeev, M.K. Haas, J.D. Jorgenson, R.J. Cava, Journal of Solid State Chemistry 169 (2002) 24–34.
[19] G.J. Thorogood, P.J. Saines, B.J. Kennedy, R.L. Withers, M.M. Elcombe, Materials Research Bulletin 43 (2008) 787–795.
[20] G. Le Flem, R. Salmon, Comptes Rendus des Seances de l'Academie des Sciences Serie C: Sciences Chimiques 271 (1970) 1182–1184.
[21] M.A. Subramanian, R. Subramanian, A. Clearfield, Solid State Ionics 15 (1985) 15–19.
[22] E. Lippmaa, A. Samoson, M. Mägi, J. Am. Chem. Soc 108 (1986) 1730–1735.
[23] M.E. Smith, Applied Magnetic Resonance 4 (1993) 1–64.

[24] A.C. Kunwar, G.L. Turner, E. Oldfield, Journal of Magnetic Resonance 124 (1986) 114–127.
[25] C.J. Howard, B.A. Hunter, A Computer Program for Rietveld Analysis of X-ray and Neutron Powder Diffraction Patterns, Lucas Heights Research Laboratories, NSW, Australia, 1998, pp. 1–27.
[26] A.J. Studer, M.E. Hagen, T.J. Noakes, Physica B—Condensed Matter 385-86 (2006) 1013–1015.
[27] R. Dupree, I. Farnan, A.J. Forty, S. El-Mashri, L. Bottyan, Journal de Physique 46 (Colloq. 8) (1985) 113.
[28] C.S. John, N.C.M. Alma, G.R. Hays, Applied Catalysis 6 (1983) 341.
[29] S.M. Bradley, J.V. Hanna, Journal of Chemical Society, Chemical Communications 1 (1993) 1249–1251.
[30] S.M. Bradley, J.V. Hanna, Journal of the American Chemical Society 116 (1993) 7771–7783.
[31] G. Paglia, C.E. Buckley, A.L. Rohl, B.A. Hunter, R.D. Hart, J.V. Hanna, L.T. Byrne, Physical Review B 68 (2003) 144110.
[32] G. Kunath-Fandrei, T.J. Bastow, J.S. Hall, C. Jäger, M.E. Smith, Journal of Physical Chemistry 99 (1995) 15138–15141.
[33] G. Kunath-Fandrei, P. Losso, H. Schneider, S. Steuernagel, C. Jäger, Solid State Nuclear Magnetic Resonance 1 (1992) 262–266.
[34] S.C. Kohn, R. Dupree, M.G. Mortuza, C.M.B. Henderson, American Mineralogist 76 (1991) 309–312.
[35] M.J. Toplis, S.C. Kohn, M.E. Smith, I.J.F. Poplett, American Mineralogist 85 (2000) 1556–1560.